Supplementary Information

Record-High Efficiency in 1.54 μm Electroluminescent Diodes Based on Lead-Free Cs_3CrBr_6: Er^{3+} Semiconductor Nanocrystals

Hanqi Xu[1], Tianyuan Wang[1], Wen Xie[1], Hao Liang[1], Hong Shen[1], Luying Wang[1], Siqi Cheng[1], Xinyu Wang[1], Yufeng Xin[1], Donglei Zhou[2], Fei Xu[1]*, and Hongwei Song[1, 2]*

[1] *Laboratory of Rare Earth Photoelectronics, Department of Physics, College of Sciences, Shanghai University, 99 Shangda Road, 200444 Shanghai, China.*

[2] *State Key Laboratory of Integrated Optoelectronics College of Electronic Science and Engineering, Jilin University, Changchun 130012, P. R. China.*

*Corresponding Author Email: *feixu@shu.edu.cn (Fei Xu); songhw@jlu.edu.cn (Hongwei Song)*

This file includes:

Supplementary Figures and Tables:

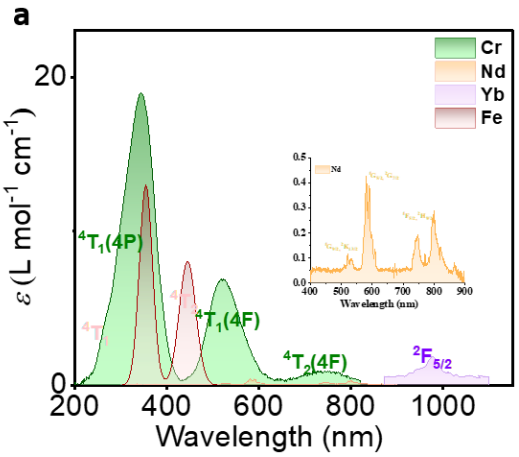

Supplementary Fig. 1 Molar extinction coefficient. Molar extinction coefficient of Cs_3XBr_6 in n-Hexane solution (X = Cr^{3+}, Fe^{3+}, Nd^{3+}, Yb^{3+}), the test was conducted using a solution of X dissolved in nitric acid and deionized water, with a concentration of 0.1 mol/L.

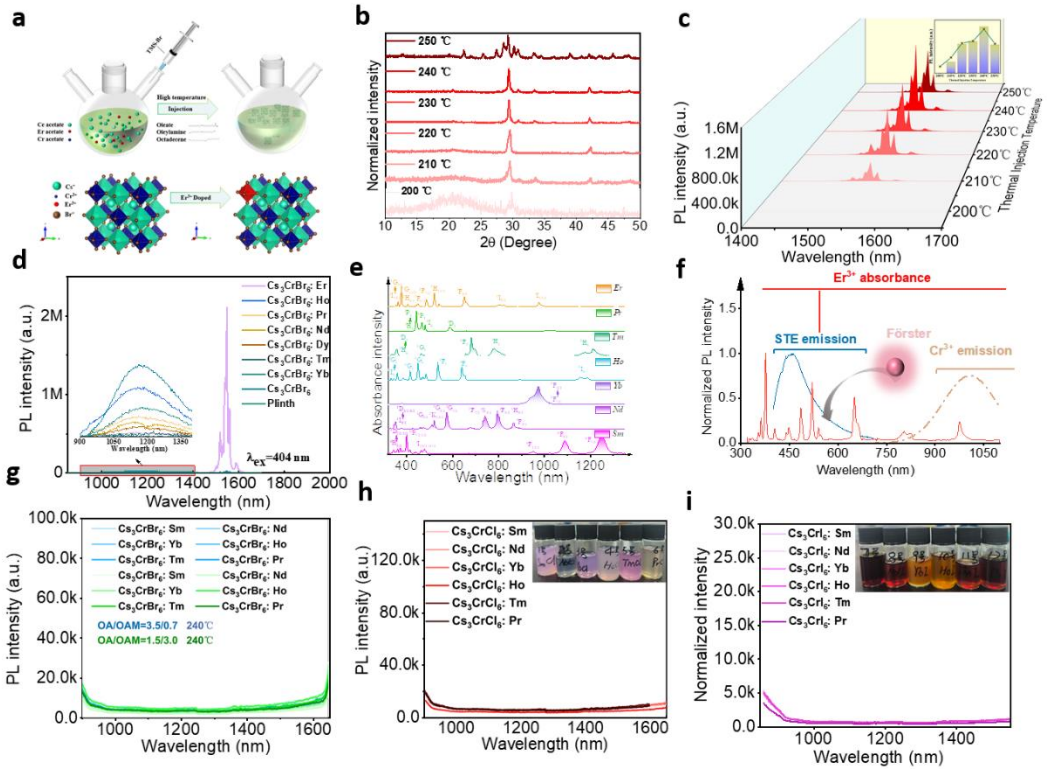

Supplementary Fig. 2 Summary of material synthesis and optical characterization. (a) Schematic illustration of the synthesis process of Cs_3CrBr_6:Er^{3+} nanocrystals. (b) and (c) Photoluminescence and XRD spectra recorded at different injection temperatures, showing the

optimal synthesis condition at 240 °C. (d) Near-infrared emission spectra of Cs_3CrBr_6 nanocrystals doped with various rare-earth ions (Tm^{3+}, Yb^{3+}, Er^{3+}), demonstrating selective sensitization only for Er^{3+}. (e) Absorption spectra of the corresponding lanthanide ions (Ln^{3+}). (f) Schematic diagram illustrating the Förster resonance energy transfer mechanism from the Cr^{3+} host to Er^{3+} emitters. (g) Near-infrared PL spectra of Cs_3CrBr_6: Er^{3+} under different oleic acid/oleylamine ratios, highlighting the effect of ligand composition on emission intensity. (h) and (i) PL spectra of Cs_3CrCl_6: Ln^{3+} and Cs_3CrI_6: Ln^{3+}, confirming the absence of detectable NIR emission for Tm^{3+} and Yb^{3+} in both chloride and iodide hosts. These results collectively establish the optimized synthesis parameters, the unique selectivity of the Cs_3CrBr_6 host toward Er^{3+}, and the Förster-type energy transfer pathway.

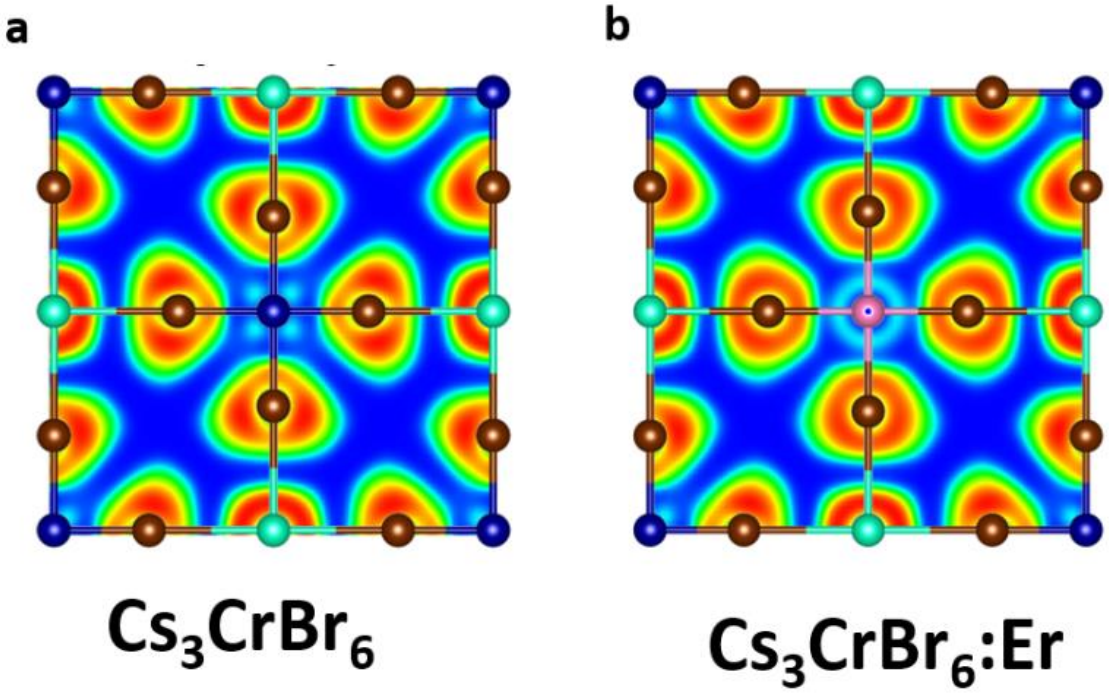

Supplementary Fig. 3 Electron localization function (ELF) analysis of Cs_3CrBr_6 before and after Er^{3+} doping. (a) ELF of undoped Cs_3CrBr_6, showing electron localization mainly within the $[CrBr_6]^{3-}$ octahedra. (b) ELF of Cs_3CrBr_6: Er^{3+}, revealing a significantly expanded electron delocalization range around the Cr^{3+} sites upon Er^{3+} incorporation. This enhanced delocalization is conducive to improved charge transport within the lattice, supporting the role of Er^{3+} in modulating the electronic structure.

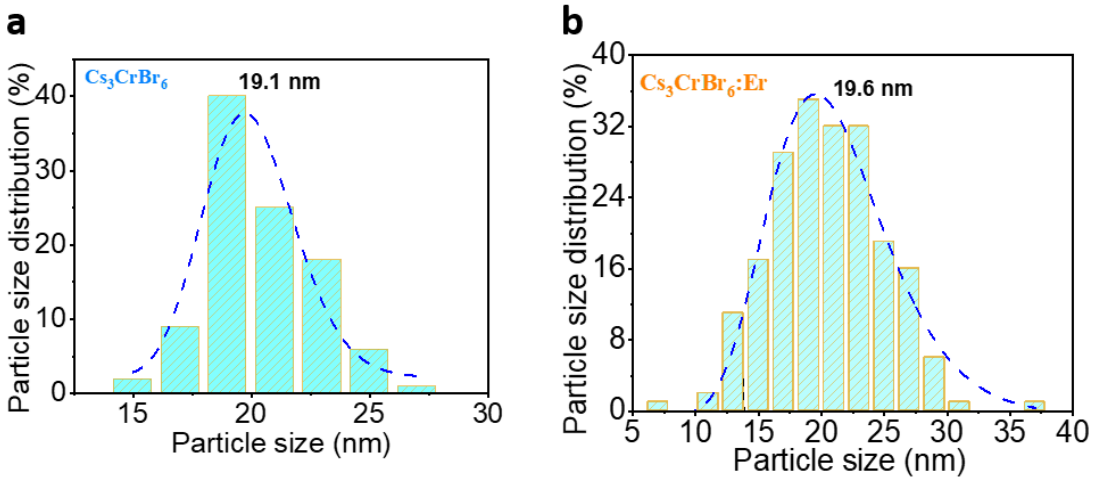

Supplementary Fig. 4 Size distribution histograms of Cs_3CrBr_6 nanocrystals before and after Er^{3+} doping. (a) Size distribution of undoped Cs_3CrBr_6 nanocrystals, with an average size of 19.1 nm and a narrow distribution. (b) Size distribution of Cs_3CrBr_6: Er^{3+} nanocrystals, showing a slightly increased average size of 19.6 nm due to lattice expansion induced by the larger ionic radius of Er^{3+}. The narrow distribution in both cases confirms the uniform morphology and good monodispersity of the synthesized nanocrystals.

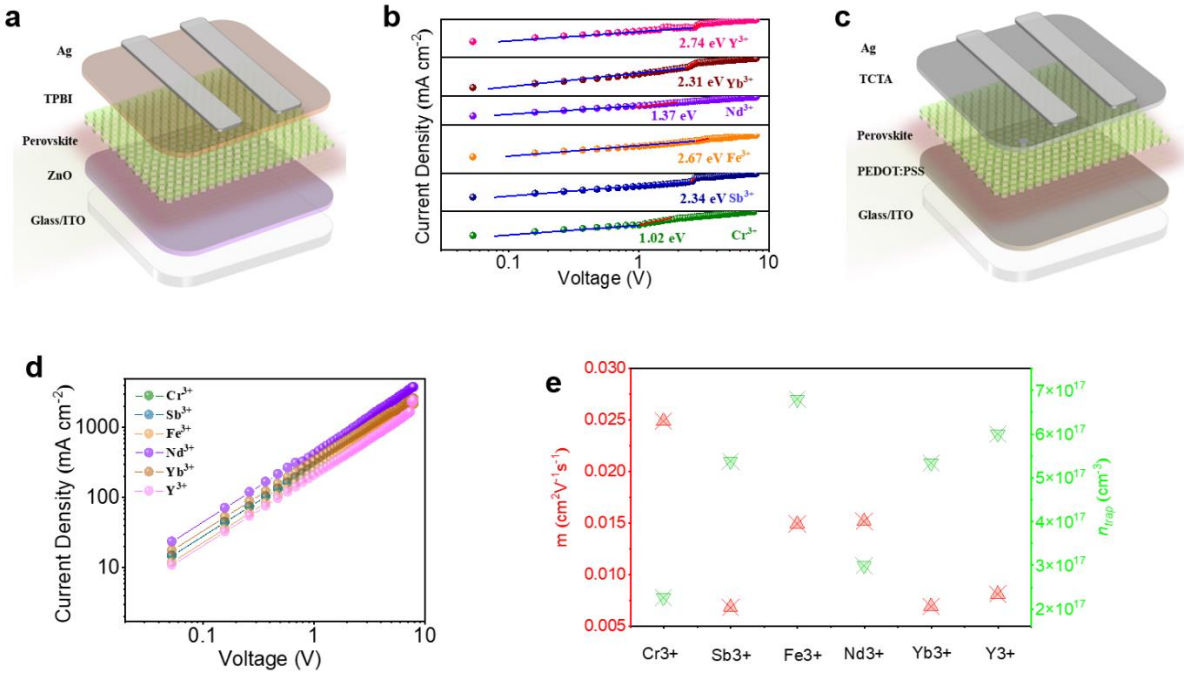

Supplementary Fig. 5 Space-charge-limited current (SCLC) measurements of Cs_3XBr_6: Er^{3+} thin films (X = Cr, Sb, Fe, Nd, Yb, Y). (a) Schematic of the electron-only device structure.

(b) Current density-voltage (J-V) curves of the electron-only devices, used to extract electron mobility and defect density. (c) Schematic of the hole-only device structure. (d) J-V curves of the hole-only devices. (e) Calculated defect densities and carrier mobilities for the different Cs_3CrBr_6: Er^{3+} compositions. The formulas for calculating carrier mobility and defect state density are provided in the main text or Supporting Information. Among all tested compositions, Cs_3CrBr_6: Er^{3+} exhibits the highest electron mobility (0.023 $cm^2 V^{-1} s^{-1}$) and a relatively low defect density, confirming its superior charge transport capability and n-type semiconducting behavior.

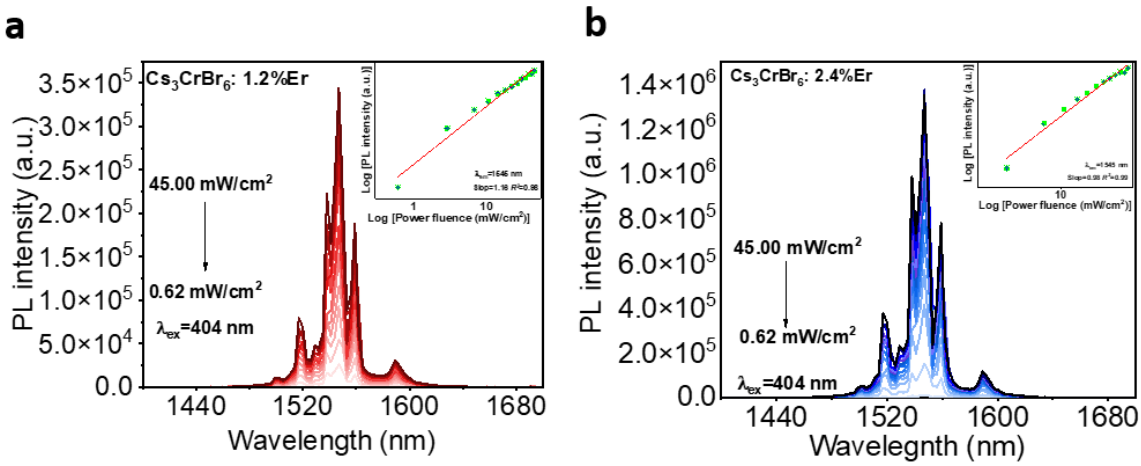

Supplementary Fig. 6 Pump power dependence of the near-infrared emission intensity for Cs_3CrBr_6: Er^{3+} nanocrystals. (a) Emission intensity as a function of excitation power density for Cs_3CrBr_6: 1.2%Er^{3+}. (b) Same for Cs_3CrBr_6: 2.4%Er^{3+}. In both cases, the emission intensity follows a nearly linear relationship with the pump power density ($I \propto P^{\alpha}$, with $\alpha \approx 1.16$ and 0.98, respectively), indicating that the down-conversion luminescence of Er^{3+} originates from a single-photon process. The fitted power coefficients are close to 1, confirming the linear nature of the sensitization pathway.

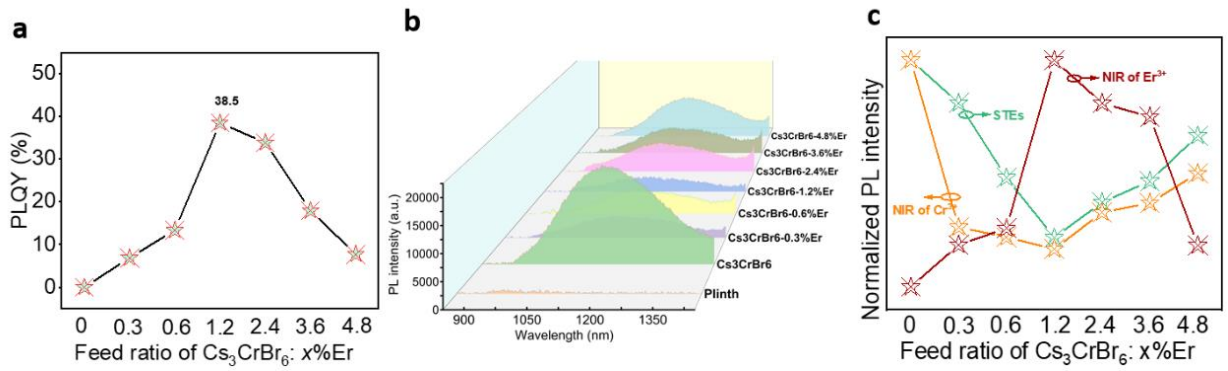

Supplementary Fig. 7 Photoluminescence quantum yield (PLQY) and emission spectra of Cs_3CrBr_6: *x*%Er^{3+} nanocrystals. (a) PLQY values as a function of Er^{3+} doping concentration. The highest PLQY of 38.5% is achieved at an optimal doping level of 1.2%, after which concentration quenching leads to a gradual decrease. (b) Weak near-infrared emission peak at approximately 1167 nm, assigned to the $^4T_2 \rightarrow {}^4A_2$ transition of Cr^{3+}. (c) Normalized emission spectra of the three luminescent centers, self-trapped excitons (STEs, blue), Cr^{3+} (green), and Er^{3+} (red). The STE emission is broad and centered at ~462 nm, the Cr^{3+} emission at ~1167 nm is much weaker, and the Er^{3+} emission at 1.54 μm is dominant after efficient energy transfer from Cr^{3+}.

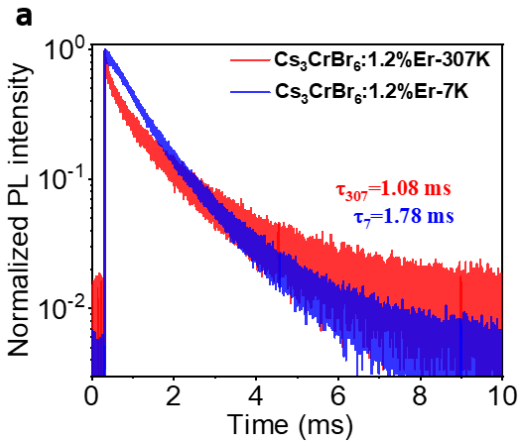

Supplementary Fig. 8 Temperature-dependent fluorescence lifetimes of Cs_3CrBr_6: 1.2%Er^{3+} nanocrystals. (a) The decay curves of the Er^{3+} 1.54 μm emission were measured at 7 K and 307 K. At 7 K, the lifetime is significantly prolonged (e.g., from 2.16 ms at 307 K to 4.76 ms at 7 K for the optimal doping), approaching the radiative limit. This strong temperature

dependence confirms that non-radiative decay channels are effectively suppressed at low temperatures, consistent with the high PLQY observed at room temperature.

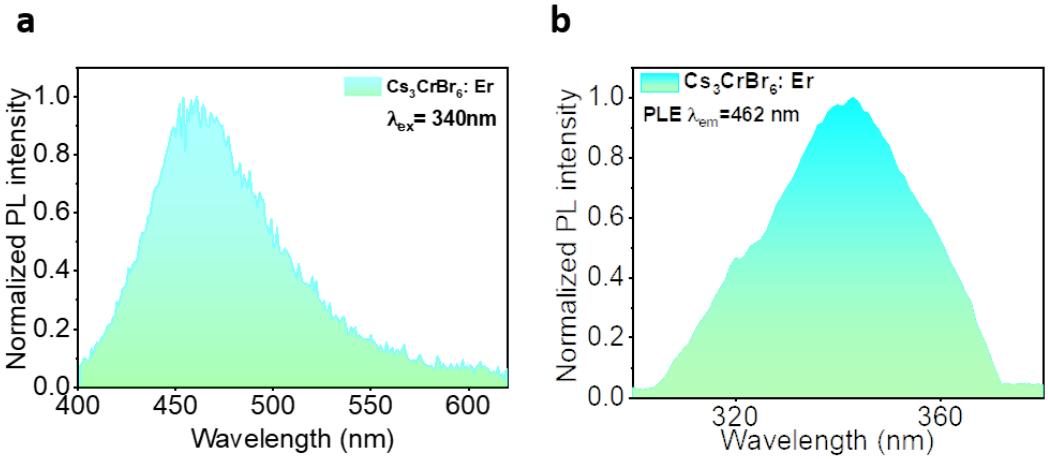

Supplementary Fig. 9 Visible photoluminescence and photoluminescence excitation spectra of Cs_3CrBr_6: Er^{3+}. (a) Visible PL spectrum of Cs_3CrBr_6: Er^{3+} under 340 nm excitation, showing a broad emission band centered at 462 nm attributed to STEs. (b) Corresponding PLE spectrum monitored at the STE emission peak (462 nm), revealing a strong band-edge absorption feature (300-400 nm) and a weaker contribution from Cr^{3+} *d-d* transitions. The overlap between the STE emission band and the absorption of Er^{3+} (Fig. 2c) provides the basis for STE-mediated energy transfer to Er^{3+}.

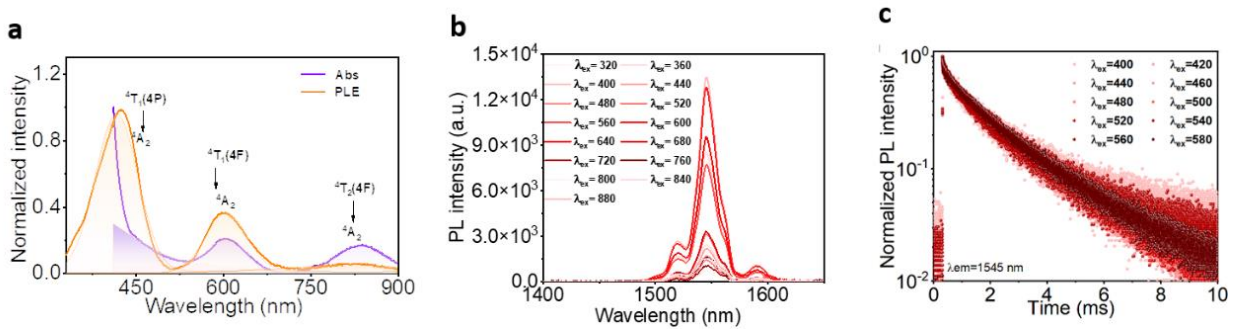

Supplementary Fig. 10 Excitation wavelength-dependent behavior of Cs_3CrBr_6: Er^{3+} at 1.54 μm emission. (a) Ultraviolet absorption and detection of PLE spectra at 1.54 um. (b) Emission intensity at 1.54 um under different excitation wavelengths. (c) The Time decay fluorescence lifetime at 1.54 um under different excitation wavelengths.

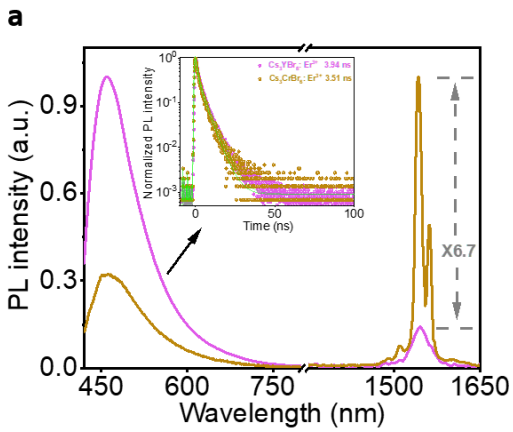

Supplementary Fig. 11 The STE emission intensity and lifetime of Cs_3YBr_6: Er^{3+} compared with those of Cs_3CrBr_6: Er^{3+}. (a) The STE emission intensity and lifetime of Cs_3YBr_6: Er^{3+} are both much higher than those of Cs_3CrBr_6:Er^{3+}, and the near-infrared emission of Er^{3+} is extremely weak, demonstrating that the Cr^{3+} *d-d* levels serve as the relay hub for energy transfer from STEs to Er^{3+}.

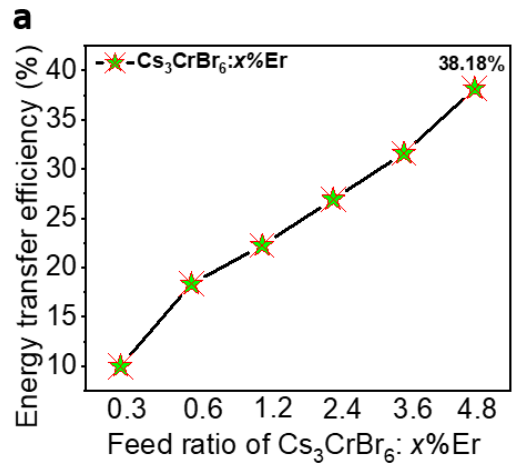

Supplementary Fig. 12 Energy transfer efficiency from the host to Er^{3+} in Cs_3CrBr_6: Er^{3+}. (a) Energy transfer efficiency as a function of Er^{3+} doping concentration.

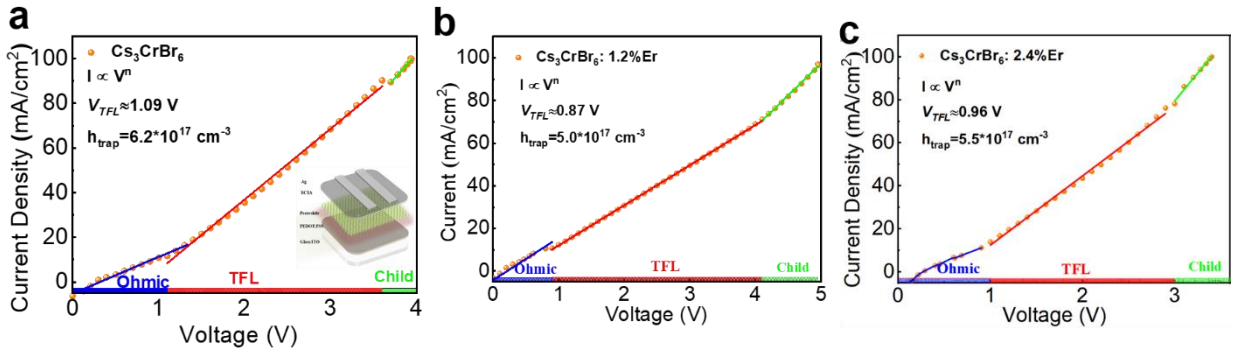

Supplementary Fig. 13 Defect state densities of Cs_3CrBr_6: Er^{3+} thin films extracted from space-charge limited current (SCLC) measurements. The defect density is plotted as a function of Er^{3+} doping concentration. For the undoped sample, N_{trap} is relatively high (6.2×10^{17} cm^{-3}). Upon introducing a low concentration of Er^{3+}, the defect density decreases significantly, reaching a minimum of 5.0×10^{17} cm^{-3} at 1.2% Er^{3+}, indicating effective defect passivation by Er^{3+} ions. Further increase of Er^{3+} concentration leads to a gradual rise in defect density due to lattice distortion and possible formation of defect clusters, but still remains lower than that of the undoped sample. These results demonstrate that optimal Er^{3+} doping not only enhances energy transfer but also reduces trap-assisted non-radiative recombination.

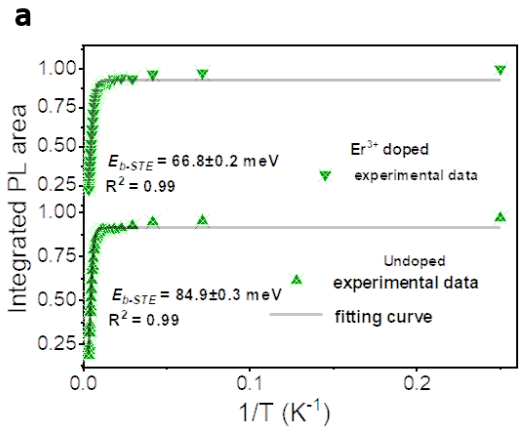

Supplementary Fig. 14 Temperature-dependent photoluminescence intensity of Cs_3CrBr_6: Er^{3+} nanocrystals. (a) The quenching is more pronounced for the STE emission, consistent with its lower exciton binding energy (84.9 meV) compared to that of the Er^{3+} emission (66.8 meV after doping). The solid lines are fits to the Arrhenius equation, yielding activation energies that confirm the enhanced thermal stability of the Er^{3+} emission upon Er^{3+} doping.

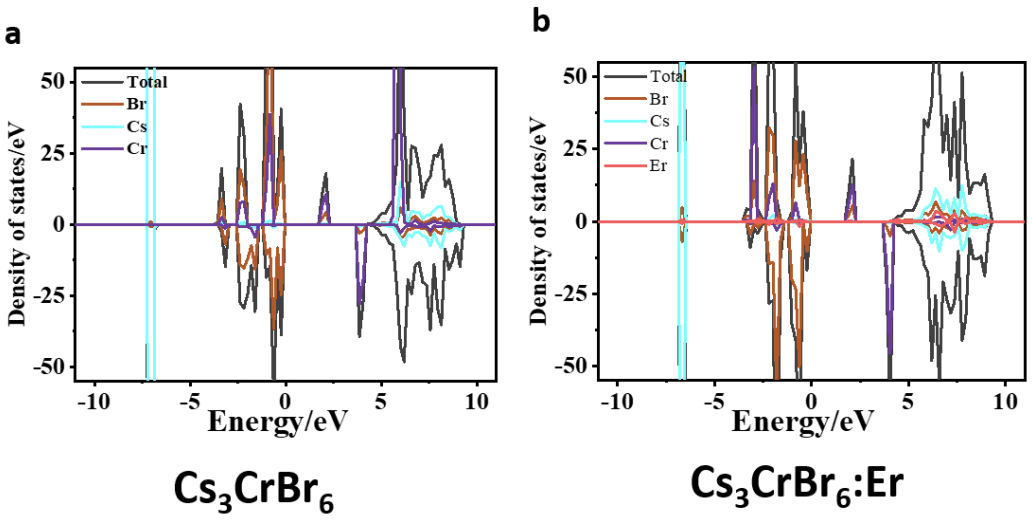

Supplementary Fig. 15 Density of states (DOS) of Cs_3CrBr_6 before and after Er^{3+} doping. (a) DOS of undoped Cs_3CrBr_6, showing that the conduction band minimum (CBM) is dominated by Cr *3d* orbitals and the valence band maximum (VBM) by Br *4p* orbitals. No contribution from Cs^+ is observed at the band edges. (b) DOS of Cs_3CrBr_6: Er^{3+}, where the overall band structure remains similar, but a slight narrowing of the band gap is observed due to Er^{3+} incorporation. The projected DOS confirms that the charge carriers are still localized within the $[CrBr_6]^{3-}$ octahedra, maintaining the inherent quantum confinement that facilitates energy transfer to Er^{3+}.

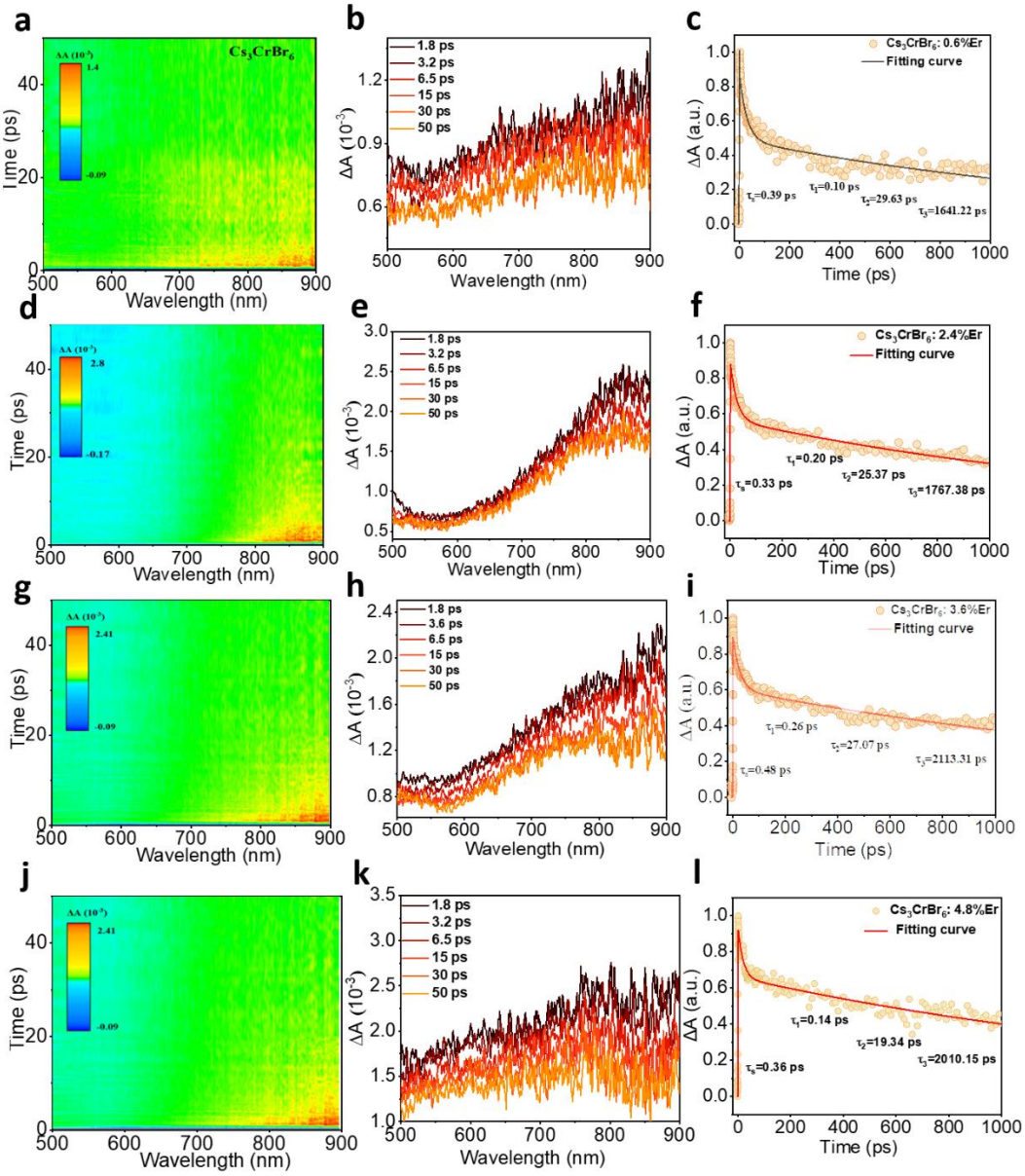

Supplementary Fig. 16 Femtosecond transient absorption (TA) spectroscopy of Cs_3CrBr_6: Er^{3+} doping concentrations (0.6%, 2.4%, 3.6%, 4.8%). (a), (d), (g), (j) pseudo-color maps of TA signals. (b), (e), (h), (k) TA spectra at selected time delays. (c), (f), (i), (l) early transient decay kinetics probed at 750 nm.

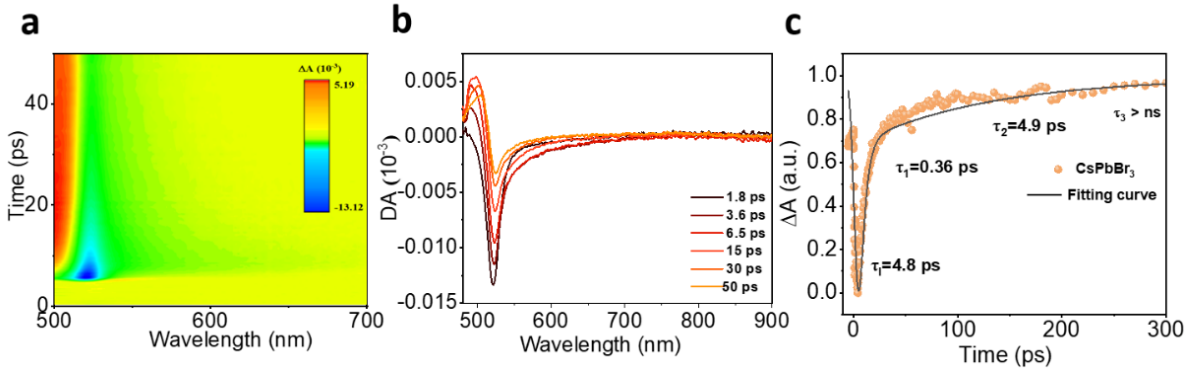

Supplementary Fig. 17 Femtosecond transient absorption (TA) spectroscopy of $CsPbBr_3$ nanocrystals. (a) Pseudo-color map. (b) spectra at selected delays. (c) early kinetics at band-edge (510 nm). $CsPbBr_3$ shows a clear ground-state bleach (GSB) with bi-exponential decay (τ_1=0.36 ps, τ_2=4.9 ps), characteristic of free excitons, in contrast to the positive PIA of Cs_3CrBr_6.

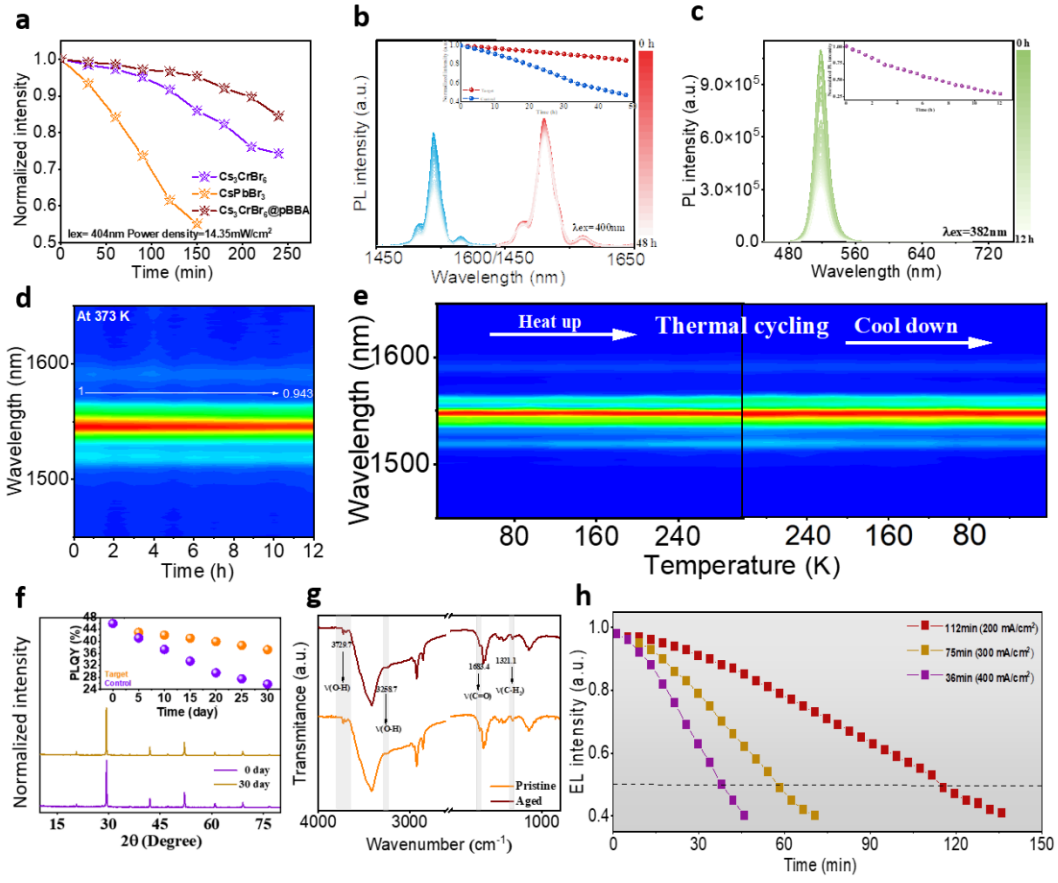

.

Supplementary Fig. 18 Comprehensive stability evaluation of pBBA-passivated Cs_3CrBr_6: Er^{3+} material system. (a) Spectral stability test comparison chart. (b) Time-dependent 1.54 μm emission intensity under 405 nm irradiation for unpassivated and passivated films. (c) comparison with $CsPbBr_3$ under 382 nm excitation. (d) 100 °C heating test. (e) thermal cycling test. (f) XRD patterns before and after storage. (g) FTIR spectra before and after aging. (h) T_{50} lifetimes at different current densities.

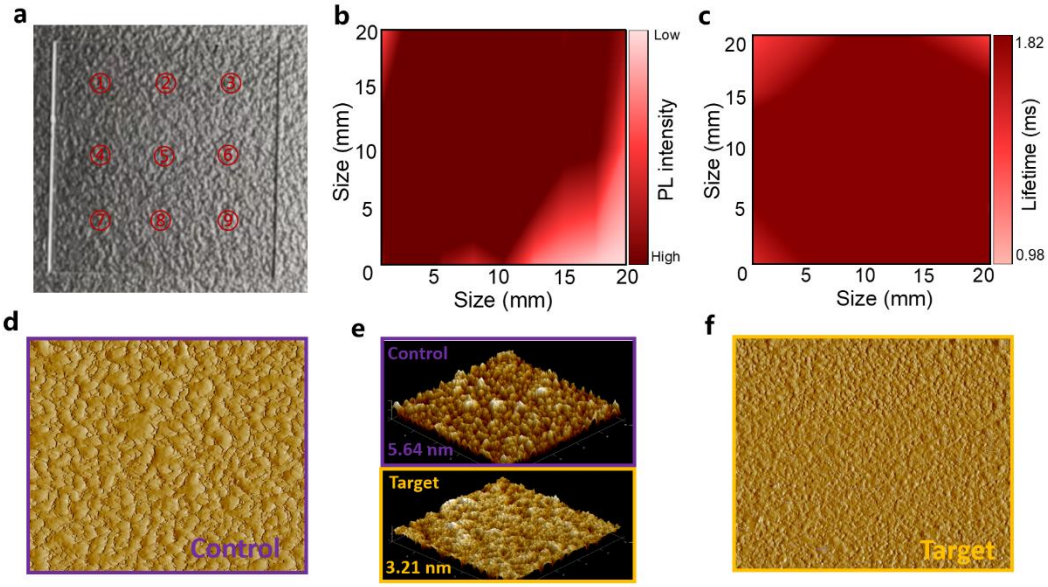

Supplementary Fig. 19 Film uniformity and surface morphology. (a) Film test location point. (b) PL intensity distribution at different points on the film. (c) Lifetime strength distribution at different points on the film. (d) Atomic force microscopy (AFM) image of the original film. (e) Roughness of AFM images of films before (5.64 nm) and after (3.21 nm) pBBA surface modification. (f) AFM image of the pBBA surface-modified film.

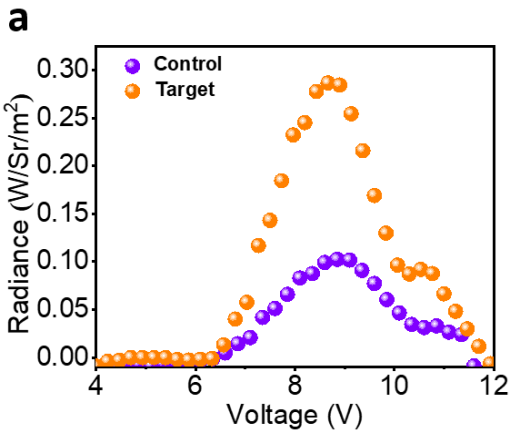

Supplementary Fig. 20 Voltage-irradiance (L-V) characteristic of the pBBA-passivated Cs_3CrBr_6: Er^{3+} NIR LED. (a) The device shows a turn-on voltage of 6.7 V and reaches a maximum radiance of 0.42 $W \cdot sr^{-1} \cdot m^{-2}$ at 8.5 V, significantly higher than that of the unpassivated device (0.11 $W \cdot sr^{-1} \cdot m^{-2}$). The improved radiance confirms the effectiveness of pBBA passivation in enhancing device performance.

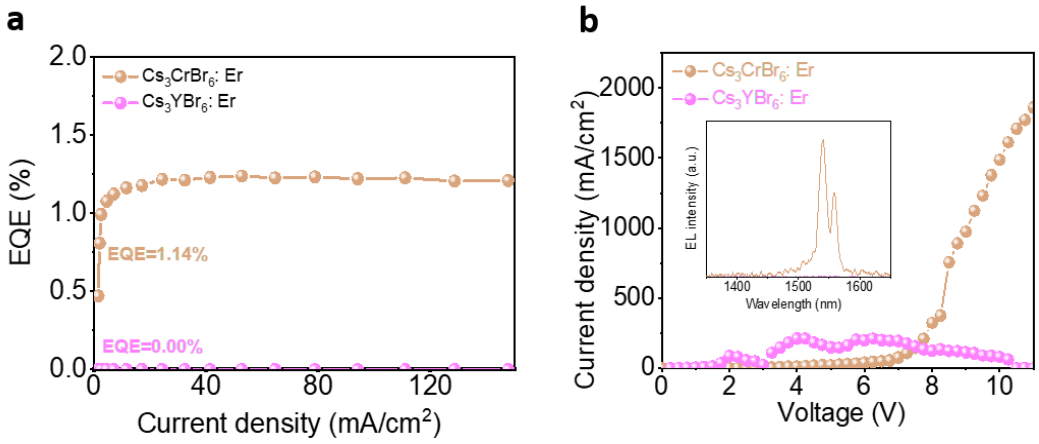

Supplementary Fig. 21 J-V characteristic without pBBA-passivated Cs_3CrBr_6: Er^{3+} and Cs_3YBr_6: Er^{3+}NIR LED. (a) Comparison of EQE of electroluminescent devices based on Cs_3CrBr_6: Er^{3+} and Cs_3YBr_6: Er^{3+}. (b) Voltage-current density curve.

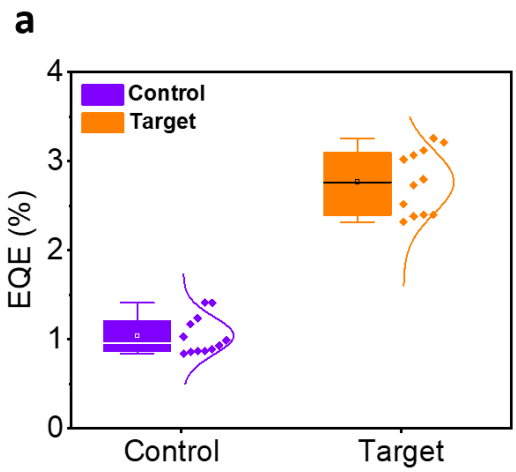

Supplementary Fig. 22 EQE distribution of 12 independently fabricated pBBA-passivated Cs_3CrBr_6: Er^{3+} NIR LEDs. (a) Statistical analysis gives an average EQE of 2.77% with a standard deviation of 0.36%, and the maximum and minimum values are 3.26% and 2.32%, respectively.

Supplementary Table 1. Inductively coupled plasma optical emission spectroscopy of Cs_3CrBr_6: 1.2%Er^{3+}. Er^{3+} concentrations were determined by ICP-OES, which provides accurate quantitative analysis of the bulk composition. The EDS signal intensities in Fig. 1d are influenced by element-dependent detection efficiencies and should not be interpreted as direct measures of concentration.

Sample number	Element measured	Instrument readings	unit	Conversion content
Cs_3CrBr_6: 1.2%Er^{3+}	Cr^{3+}	0.8064	mg/L	29734.51
Cs_3CrBr_6: 1.2%Er^{3+}	Cs^{3+}	12.2840	mg/L	452949.85
Cs_3CrBr_6: 1.2%Er^{3+}	Er^{3+}	2.1690	mg/L	1599.56
Actual Doping Concentration				**0.28%**
Feed Ration				**1.2%**

Supplementary Table 2. NIR Emission PLQY of Er^{3+}-Doped Halide Perovskites.

Compounds	Status	Excitation	PLQY	Ref.
$Cs_2NaSbCl_6$: Er^{3+}	NCs	280 nm	0.26%	[1]
$Cs_2Ag_{0.1}Na_{0.9}BiCl_6$: Er^{3+}	MCs	365 nm	4.5%	[2]
$Cs_4CdSb_2Cl_{12}$: Er^{3+}	NCs	390 nm	16.7%	[3]
$Cs_4CdBi_2Cl_{12}$: Mn^{2+}/Er^{3+}	MCs	370 nm	18%	[4]
Cs_3DyI_6: Er^{3+}	NCs	365 nm	21.5%	[5]
$Cs_2NaBiCl_6$: Fe^{3+}/Er^{3+}	MCs	365 nm	22.5%	[6]
$Cs_2NaScCl_6$: Er^{3+}	MCs	380 nm	25.6%	[7]
$Cs_2AgInCl_6$: $Bi^{3+}/Yb^{3+}/Er^{3+}$	NCs	365 nm	26.6%	[8]
$Cs_2AgInCl_6$: Cr^{3+}/Er^{3+}	NCs	356 nm	29%	[9]
$Cs_2NaBiCl_6$: Mo^{3+}/Er^{3+}	MCs	450 nm	34.8%	[10]
$Cs_2Ag_{0.6}Na_{0.4}InCl_6$: Bi^{3+}/Er^{3+}	MCs	365 nm	38.26%	[11]

Cs_3CrBr_6: Er^{3+}	NCs	400 nm	38.5%	This work

Supplementary Table 3. The fitting results of PIA signal curves and the positions of photoinduced absorption.

Compounds	τs (ps)	τ1 (ps)	τ2 (ps)	Abs bands (nm)
Cs_3CrBr_6	0.35	0.21	43.59	751
Cs_3CrBr_6: 0.6%Er^{3+}	0.39	0.10	29.63	753
Cs_3CrBr_6: 1.2%Er^{3+}	0.23	0.13	19.45	858
Cs_3CrBr_6: 2.4%Er^{3+}	0.33	0.20	25.37	848
Cs_3CrBr_6: 3.6%Er^{3+}	0.48	0.26	27.07	792
Cs_3CrBr_6: 4.8%Er^{3+}	0.36	0.14	19.34	765

Supplementary Table 4. Comparison table of Cs_3CrBr_6: Er^{3+} with state of the art lanthanide-based luminescent systems.

Property	Sensitized Nanoparticles	Sensitized Organic Complexes	This Work (Cs_3CrBr_6: Er^{3+})
All-inorganic	√	×	√
Luminous efficacy (1.54 um, downconversion)	0.03% [12]	13% [13]	38.5%
Electrical conductivity	×	×	√
Direct band gap host	×	×	√
Demonstrated LED device (EQE)	0.004% [12]	0.011% [14]	3.26%

Supplementary Table 5. A Comparative Performance Study of Er^{3+}-Doped NIR-EL Devices in Diverse Material Platforms.

Compounds	Device Structure	Turn-on Voltage [V]	EQE (%)	T50[min]	Ref
Rare-earth complex	ITO/ CuPc/ [(Erhfaa)$_3$ (bpy)]: CBP/ BCP/ AlQ_3/ LiF/ Al	8	0.0011	N/A	[14]
Rare-earth oxide	Si/ YGG:Er/ TiO_2/ Al_2O_3/ ZnO/ Al	30	**2.5**	2000	[15]
$Cs_2AgInCl_6$: $Bi^{3+}/Yb^{3+}/Er^{3+}$	ITO/ PEDOT: PSS/ $Cs_2AgInCl_6$: $Bi^{3+}/Yb^{3+}/Er^{3+}$/ TPBi/ LiF/ Ag	7.2	**1.79**	198	[8]
$CsPbCl_3$: Yb^{3+}/Er^{3+}	ITO/ PEDOT: PSS/ $CsPbCl_3$: Yb^{3+}/Er^{3+}/ TPBi/ LiF/ Ag	1.4	**0.366**	2	[16]
(PEA, Cs) Pb (Cl, Br)$_3$: Yb^{3+}/Er^{3+}	ITO/ PEDOT: PSS/ (PEA, Cs) Pb (Cl, Br)$_3$: Yb^{3+}/Er^{3+}/ TPBi/ LiF/ Ag	4.75	**1.96**	17	[17]
Cs_3DyI_6:Er^{3+}	ITO/ ZnO/ Cs_3DyI_6:Er^{3+}/ TCTA/ MoO_3/ Ag	6.5	**2.76**	345	[5]
Cs_3CrBr_6:Er^{3+}	ITO/ ZnO/ LiF/ Cs_3CrBr_6:Er^{3+}/ TCTA/ MoO_3/ Ag	6.7	**3.26**	138	This work

Supplementary References

1. Wu R. et al. All-Inorganic Rare-Earth-Based Double Perovskite Nanocrystals with Near-Infrared Emission. *Laser & Photonics Reviews*. **15**, 1-7 (2021).
2. Zhang H. et al. Boosting the 1540 nm Near-infrared Luminescence of Er^{3+} Doped Double Perovskites via Cross-relaxation and Energy Transfer. *Ceramics International*. **49**, 18068-18075 (2023).
3. Cai T. et al. Lanthanide Doping into All-Inorganic Heterometallic Halide Layered Double Perovskite Nanocrystals for Multimodal Visible and Near-Infrared Emission. *Journal of the American Chemical Society*. **146**, 3200-3209 (2024).
4. Dang P. et al. Red–NIR Luminescence in Rare-Earth and Manganese Ions Codoped $Cs_4CdBi_2Cl_{12}$ Vacancy-Ordered Quadruple Perovskites. *Chemistry of Materials*. **35**, 1640-1650 (2023).
5. Wang T. et al. Breaking Efficiency Barrier: Dual-Channel Energy Transfer Enables Record 1540 nm NIR LEDs from Er^{3+}-Doped Cs_3DyI_6 Nanocrystals. *Advanced Materials*. **38**, e12712 (2026).
6. Wang Y. et al. Enhancement of NIR-II Emission of Er^{3+} by Doping Fe^{3+} in Double Perovskites: Multimode Luminescence for Versatile Optoelectronic Applications. *Angewandte Chemie International Edition*. **64**, e202416021 (2024).
7. Zhao C. et al. An Er^{3+}-Doped $Cs_2NaScCl_6$ Lead-Free Double Perovskite with Efficient Broadband Visible to Near-Infrared Emission and Multimodal Upconversion Luminescence. *The Journal of Physical Chemistry Letters*. **14**, 9011-9018 (2023).
8. Song R. et al. Broadband Emission-Enabled Energy Transfer in Double Perovskites for Efficient Er^{3+}-Driven Long-Wavelength Near-Infrared Optoelectronics. *Laser & Photonics Reviews*. **19**, 1-11 (2025).
9. Gan W. et al. Broad-Band Sensitization in Cr^{3+}–Er^{3+} Co-Doped $Cs_2AgInCl_6$ Double Perovskites with 1.5 μm Near-Infrared Emission. *Chemistry of Materials*. **35**, 5291-5299 (2023).
10. Wang Z. et al. Enhancement of Blue-Light-Excited NIR-II Emission of Er^{3+} in Double Perovskites via Mo^{4+} Sensitization. *Laser & Photonics Reviews*. **20**, 1-10 (2025).
11. Zhao J. et al. Efficient Dual-mode Emissions of High-concentration Erbium Ions Doped Lead-free Halide double Perovskite Single Crystals. *Journal of Alloys and Compounds*. **895**, 162601-1627610 (2022).
12. Yu Z. et al. Triplets electrically turn on insulating lanthanide-doped nanoparticles. *Nature*. **647**, 625-631 (2025).
13. Li H. et al. Correction: Enhanced 1.54 μm luminescence of a perfluorinated erbium complex sensitized by perfluorinated Pt(ii) and Zn(ii) phthalocyanines with 980 nm emission. *Journal of Materials Chemistry C*. **9**, 1107-1107 (2021).
14. Ahmed Z, Iftikhar K. Variant Coordination Sphere, for Efficient Photo- and Electroluminescence of 0.4–1.8μm, of Lanthanide(III) Complexes Containing a β-diketone Ligand with Low Vibrational Frequency C–F Bonds and a Flexible 2,2′-bipyridine Ligand. *Polyhedron*. **85**, 570-592 (2015).
15. Yu Z. et al. Polycrystalline Er-doped $Y_3Ga_5O_{12}$ Nanofilms Fabricated by Atomic Layer Deposition on Silicon at a Low Temperature and the Exploration on Electroluminescence Performance. *Nanoscale*. **14**, 10540-10548 (2022).

16. Li H. et al. Realization of 1.54-μm Light-Emitting Diodes Based on Er^{3+}/Yb^{3+} Co-Doped $CsPbCl_3$ Films. *Advanced Materials*. **35**, 1-12 (2023).
17. Li W. et al. Energy Funnel-Driven Quantum Cutting in Yb^{3+}/Er^{3+}-Doped Quasi-2D Perovskites Enables High-Efficiency Dual-Band Near-Infrared Light-Emitting Diodes. *Advanced Functional Materials*. **35**, 1-10 (2025).